Symmetry-Based Modeling and Hybrid Orientation-Force Control of Wearable Cutaneous Haptic Device

Somang Lee, Hyunsu Kim and Dongjun Lee

Abstract— We propose novel symmetry-based modeling and hybrid orientation-force control frameworks for cutaneous haptic device (CHD) to generate precise three degree-of-freedom (DoF) contact force on the fingertip robustly against user variability. The CHD hardware is designed in a form of an underactuated cable-driven parallel mechanism, with springs placed along the tendon to stabilize the pose. We analyze the kinematics of the CHD and propose a pose estimator by exploiting the symmetrical nature of the mechanism. We then devise a hybrid orientation-force controller to track the direction and magnitude of the desired contact force simultaneously in a feedback manner for control accuracy and robustness. We also adopt a tension regulator to mitigate friction effect during the actuation. Experimental validation and demonstration show the efficacy of the CHD with our proposed estimation and control framework.

I. INTRODUCTION

Wearable haptic devices have emerged as a promising technology in the fields of virtual reality (VR) and robotics for enhancing the user experience by providing tactile stimuli such as pressure [1], vibration [2], or reaction force [3]. Cutaneous haptic devices (CHDs), in particular, are advantageous in providing efficient and informative tactile feedback by stimulating the receptors of the skin to mimic the sensation of touch [4]. Unlike other kinesthetic haptic devices, which typically require bulky and complex actuators, wearable CHDs can be designed to be small and portable so that they have a potential to provide a more natural and immersive haptic experience for a variety of applications in a cost-effective manner.

For high-performance and robust contact force generation through a wearable CHD, accurate state information of the device and feedback control based on that are essential. However, the limited sensing capabilities due to, and the complex kinematics/mechanics within, the small size of wearable CHDs make this estimation/control problem difficult. Perhaps, the simplest way to control a wearable CHD is based on the position control [5]–[10], that is, given the target fingertip force, compute the desired pose of the end-effector based on some fingertip compliance model, and position-control the device to attain that desired pose. These methods, however, are not so robust against uncertainty, disturbance
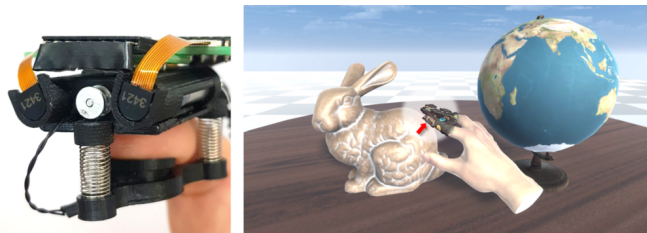
Fig. 1. The wearable CHD to generate a three-DoF contact force (left), and an application of our proposed control framework to explore the shape of a virtual object (right).

or inter-user variability (e.g., inaccurate contact force due to complex fingertip mechanics [11] or different fingertip sizes), as typical when the position control is used for interaction.

To overcome this issue of position control, the works of [12], [13] adopt fingertip force sensing capability and propose admittance-type force control for wearable CHDs, that is, real-time measure the fingertip force, compute the desired device pose based on some fingertip interaction model such as compliance, and realize that desired pose via some low-level position control. Their adoption of force sensing is advantageous for robustness, yet, at the same time, their relying on the fingertip models, particularly for the pose estimation purpose [12], on which the control is based, can be detrimental.

In this paper, we propose a novel hybrid orientation-force control for cable-driven wearable CHD to generate three-degree-of-freedom (DoF) contact force at the fingertip accurately and robustly with direct contact force sensing. We first model the kinematics of our proposed CHD (see Fig. 1 and Fig. 2) based on its symmetrical nature, that is, the upper and lower parts of the CHD device are moving while maintaining geometric symmetry w.r.t. a certain virtual plane and the contact force is normal to that plane (Sec. III-A). This symmetry of the CHD has been confirmed through our experimental evaluations. We also modified the CHD hardware from [14] to be consistent with this symmetry property. This symmetry-based modeling not only greatly simplifies the kinematics analysis of the CHD, but also enables us to accurately estimate the device (i.e., contact part) pose and precisely decompose the CHD kinematics along the orientation and force control directions, all crucial for the development of our hybrid orientation-force control (i.e., align the 2-DoF orientation of the contact part and push it to the desired force magnitude simultaneously while utilizing estimated pose and sensed force). To mitigate the frictional effect during the actuation, we also adopt a tension regu-

lator. The performance of the proposed control framework is experimentally verified and an illustrative application is presented.

Our previous work [14] also proposes modeling and control scheme for a similar wearable CHD with direct contact force measurement and no fingertip model. The theory of [14], however, is limited to the case where there are no horizontal and yaw motions of the contact part. The control in [14] also exhibits poorer performance, as it is injecting mixed commands both to the orientation and force control channels. In contrast, in this paper, by utilizing the symmetry-based modeling, we can precisely decompose the device kinematics along the two control objectives and apply the hybrid orientation-force control for each of them with no crosstalk between them. We allow the horizontal and yaw motions as well differently from [14]. To our knowledge, this paper presents and implements the hybrid orientation-force control for wearable CHDs for the very first time.

The rest of the paper is organized as follows. Sec. II presents the design of the CHD hardware. Sec. III describes the kinematics analysis, system modeling, and controller development for the CHD. Sec. IV presents the performance evaluation for the proposed CHD and its control framework. Sec. V presents an illustrative application of the CHD. Sec. VI concludes the paper with some comments on future research directions.

II. CHD Hardware Design

The CHD is designed in a form of a three-DoF under-actuated cable-driven parallel mechanism as shown in Fig. 2: the base part is fixed on the distal phalanx of a finger, and the contact part is suspended and contacts the fingertip as the wires pull. On the base part, three DC-micromotors (Faulhaber, 0615S, 64:1 gear ratio) with incremental encoders (Faulhaber, HXM3-64) are mounted, one heading in the opposite direction to the other two, forming an isosceles triangle with the fingertip placed inside. For each motor shaft, a pulley ($\phi = 4$ [mm]) with a wire is coupled to transmit the tension to the contact part and passes through the inside of the spring support ($k = 0.05$ [N/mm]). The springs not only stabilize the pose of the parallel mechanism but also prevent slacking, allowing each wire to be driven by just one actuator. We carefully select parameters for the spring (e.g., free length, external diameter, wire diameter, spring constant) to ensure sufficient interior space for the fingertip and prevent buckling while the springs are compressed and bent. As will be discussed in Sec. III-A, the latter is an essential condition for the kinematics analysis.

The contact part consists of two layers: a lower layer pulled through the wires and an upper layer generating a contact force by pressing the fingertip. Between the two layers are an FSR sensor (Interlink, FSR 400) to measure the magnitude of the contact force and three springs that keep the layers apart when there is no contact force. Since the maximum travel length of these springs is sufficiently small, the relative rotation between the two layers is negligible. The top surface of the upper layer is concave to fit the shape of
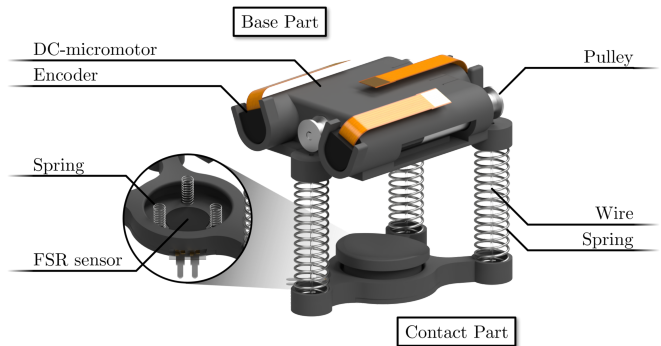

Fig. 2. Hardware design of the wearable CHD for rendering three-DoF contact force.

the fingertip so that the contact part does not slip when tilted and to press the fingertip firmly. This is a necessary condition for the modeling in Sec. III-B of the contact force applied to the contact part.

Except for DC-micromotors, pulleys, wires, springs, and an FSR sensor, all the other parts consisting of the device are 3D-printed. The total size of the device is $43.6 \times 32.4 \times 19.5$ [mm^3] with the springs fully compressed (the maximum travel length of the spring is 18.5 [mm]), and the weight is 30 [g]. Our design requires no adhesive for assembly except for the two layers of the contact part, which increases the ease of repair or replacement.

III. CHD Control Design

A. Kinematics Analysis

To derive forward kinematics of the CHD (i.e., given wire lengths, find pose of the contact part), let us first consider the contactless case, for simplicity. This analysis can be extended to contact case, as will be discussed in Sec. III-B. We simplify the geometry of the base and contact parts of the CHD to triangles on each plane with vertices $\mathcal{V}_{B_i}, \mathcal{V}_{C_i}, i \in \{1, 2, 3\}$ at the endpoints of each wire path, where the coordinate frames $\{B\}$ and $\{C\}$ are attached on each plane as shown in Fig. 3. When attaching $\{B\}$ (resp., $\{C\}$), we define its basis vector e_1 to be aligned in $p^B_{O_B, \mathcal{V}_{B_1}}$ (resp., $p^B_{O_C, \mathcal{V}_{C_1}}$) direction and another basis vector e_3 in the normal direction of its attached plane, where $p^Z_{X,Y} \in \Re^3$ represents the vector from X to Y expressed in $\{Z\}$-frame. We often abuse the notation of coordinate frames such as $\{B\}$, $\{C\}$ to denote the attached planes, unless there is confusion. Given three wire lengths $l = \begin{bmatrix} l_1; & l_2; & l_3 \end{bmatrix} \in \Re^3$, the pose of the contact part is in a three-dimensional unactuated space. In this unactuated space, the springs along each wire induce the contact part to converge into the stable pose due to the principle of minimum potential energy. However, since the springs not only compress but also bend, it is burdensome to compute the forces of all springs to solve the statics. There are studies on the kinematic analysis for similar mechanisms [15], [16], yet unlike those which have only one spring in the center, our CHD needs to consider three springs simultaneously.
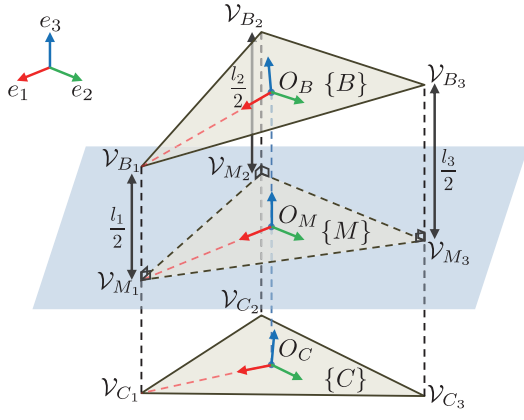
Fig. 3. Definitions of frames and vertices for the kinematic analysis of the CHD, including the plane of symmetry colored in blue.
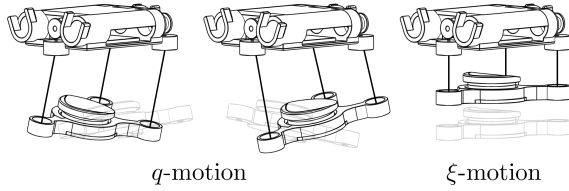

q-motion $\qquad$ ξ-motion

Fig. 4. Three-DoF motion of the CHD. For each motion, $\{B\}$ and $\{C\}$ maintain plane symmetry w.r.t. $\{M\}$.

To circumvent this complex problem, we exploit the symmetrical nature of the device mechanism. Due to the design of our CHD hardware, we have $\triangle \mathcal{V}_{B_1} \mathcal{V}_{B_2} \mathcal{V}_{B_3} \equiv \triangle \mathcal{V}_{C_1} \mathcal{V}_{C_2} \mathcal{V}_{C_3}$. Assuming no buckling of springs, the potential energy is minimized when there is no additional deformation other than being compressed by the reduced wire length and bent along the same axis. In this configuration, the two triangles on $\{B\}$ and $\{C\}$ are always plane-symmetric to a certain virtual plane $\{M\}$ (see Fig. 3), and we can simplify the kinematics analysis by introducing that plane of symmetry, where its origin O_M and the associated vertices $\mathcal{V}_{M_i}$ are projections of those at $\{B\}$ and $\{C\}$ onto $\{M\}$. Considering $\{M\}$ fixed, the three-DoF motions of $\{B\}$ and $\{C\}$ are 1) contracting or expanding together in a direction normal to $\{M\}$, and 2) rolling or pitching by opposite angles, as shown in Fig. 4. The suitability of this assumption is verified experimentally in Sec. IV-A. Here, noting that O_B or O_C can be located anywhere as long as the symmetry is preserved, we locate O_C at the contact point of the fingertip on the lower plane, and define $a_i \in \Re, a_i > 0, i \in \{1, 2, 3\}$ satisfying $\sum_i a_i p_{O_{(\cdot)}, \mathcal{V}_{(\cdot)_i}}^{(\cdot)} = 0$ with $\sum_i a_i = 1$.

Now, we can specify the pose of $\{M\}$ (i.e., p_{O_B, O_M}^B and R_{BM}^B) using the following relations:

$$p_{\mathcal{V}_{B_i}, \mathcal{V}_{M_i}}^B = -\frac{l_i}{2} R_{BM}^B e_3, \qquad i \in \{1, 2, 3\} \quad (1)$$

$$p_{O_B, O_M}^B = \sum_i a_i (p_{O_B, \mathcal{V}_{B_i}}^B + p_{\mathcal{V}_{B_i}, \mathcal{V}_{M_i}}^B - p_{O_M, \mathcal{V}_{M_i}}^B)$$
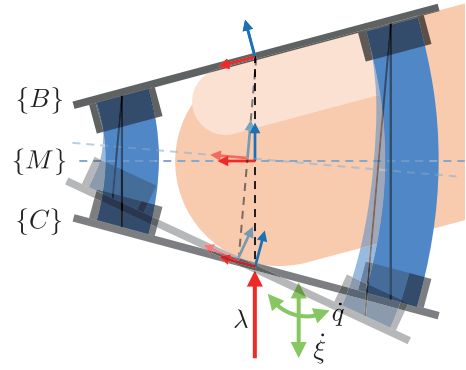$$\overset{=}{\underset{(1)}{}} -\sum_i a_i \frac{l_i}{2} R_{BM}^B e_3 \quad (2)$$

Fig. 5. Schematic diagram of the CHD when the fingertip is in contact. Since the wire tension and the contact force acts normal to $\{M\}$, the contact point O_C can translate horizontally when $\{M\}$ is tilted.

where $R_{BM}^B \in \mathrm{SO}(3)$ represents the rotation of $\{M\}$ w.r.t. $\{B\}$. To calculate R_{BM}^B, combining (1) and (2), we obtain

$$(p_{O_B, \mathcal{V}_{B_i}}^B)^T R_{BM}^B e_3 = \frac{1}{2} \left[l_i - \sum_j a_j l_j \right], \quad i \in \{1, 2, 3\}$$

Since this linear relation has rank 2, we can erase one of these equations (here, the third one) and get

$$\begin{bmatrix} (p_{O_B, \mathcal{V}_{B_1}}^B)^T \\ (p_{O_B, \mathcal{V}_{B_2}}^B)^T \end{bmatrix} R_{BM}^B e_3 = \frac{1}{2} \underbrace{\begin{bmatrix} 1 - a_1 & -a_2 & -a_3 \\ -a_1 & 1 - a_2 & -a_3 \end{bmatrix}}_{=: J \in \Re^{2 \times 3}} l \quad (3)$$

to find $R_{BM}^B e_3$. The remaining one-DoF for R_{BM}^B can be resolved by the following equation

$$(p_{O_B, \mathcal{V}_{B_1}}^B)^T R_{BM}^B e_2$$
$$= (p_{O_B, O_M}^B + p_{O_M, \mathcal{V}_{M_1}}^B - p_{\mathcal{V}_{B_1}, \mathcal{V}_{M_1}}^B)^T R_{BM}^B e_2 \underset{(1),(2)}{=} 0$$

which is related to the yaw-rotation of $\{M\}$ and has no effect on R_{BC}^B (i.e., only the term Jl determines the orientation of $\{C\}$). Therefore, we can introduce the following configuration space decomposition:

$$l = J^\dagger q + N_J \xi \quad (4)$$

where $J^\dagger := J^T (JJ^T)^{-1} \in \Re^{3 \times 2}$ and $N_J \in \Re^{3 \times 1}$ is the kernel of J so that $q = Jl$. Here, note that 1) the motion of the contact part can be decoupled into rotation-related q-motion and its complement ξ-motion (see Fig. 4), and 2) the ξ-motion is in the normal direction of $\{M\}$, not $\{C\}$.

Finally, the pose of $\{C\}$ can be obtained by simply doubling the pose of $\{M\}$ w.r.t. $\{B\}$ (i.e., $p_{O_B, O_C}^B = 2 p_{O_B, O_M}^B$, $R_{BC}^B = R_{BM}^B R_{BM}^B$). Therefore, using this decomposition (4), we can estimate the pose of the contact part of the CHD for given l.

B. System Modeling

When the contact part touches the fingertip, a Pfaffian constraint arises to prevent the contact part from penetrating

the finger, and the contact force is generated as the wires are pulled tighter. This constraint can be written as

$$0 = (R_{BM}^B e_3)^T \dot{p}_{O_B,O_C}^B = -\sum_i a_i \dot{l}_i = -\underbrace{\begin{bmatrix} a_1 & a_2 & a_3 \end{bmatrix}}_{=:A \in \Re^{1\times 3}} \dot{l} \tag{5}$$

using (2). Note that this constraint prevents motion in the e_3-direction of $\{M\}$, not $\{C\}$ since the contact part can move in the horizontal direction (see Fig. 4 and Fig. 5). Using the following equation, we can see that when the three tensions $u \in \Re^3$ of each wire is in the A^T-direction, no moment is generated around O_C and only the Pfaffian constraint force changes.

$$\sum_i (p_{O_C,\mathcal{V}_{C_i}}^M \times a_i \operatorname{vec}(p_{\mathcal{V}_{C_i},\mathcal{V}_{B_i}}^M))$$
$$= \sum_i (a_i(p_{O_C,O_M}^M + p_{O_M,\mathcal{V}_{M_i}}^M - p_{\mathcal{V}_{C_i},\mathcal{V}_{M_i}}^M) \times e_3)$$
$$= \sum_i a_i p_{O_M,\mathcal{V}_{M_i}}^M \times e_3 = 0$$

To formulate the system modeling of the CHD, we assume that the Pfaffian constraint force corresponding to the constraint (5) can fully represent the contact force $f^B \in \Re^3$ as

$$f^B = \lambda R_{BM}^B e_3$$

where $\lambda \in \Re$ is the associated Lagrange multiplier of the constraint (5) (i.e., f^B is not normal to the plane $\{C\}$, but $\{M\}$). This assumption holds as long as the concave curvature of the top surface of the contact part remains in contact with the fingertip without slip, and no pushing force is generated in the other direction by local skin compression. Note that the contact part is simplified to be a plane in Fig. 5, but the geometry of the upper layer can still press the fingertip in the direction the wires pull even when tilted. We also neglect some small forces such as gravity and reaction forces at the spring housings. Then we can extend the analysis of the contactless case discussed earlier since the contact force only acts normal to $\{M\}$, and the quasi-static equation for the contact part of the CHD is given as follows:

$$A^T \lambda = K(q)(l - l_0) + u$$
$$= K(q)[J^\dagger(q - q_0) + N_J(\xi - \xi_0)] + u \tag{6}$$

where $\lambda = f/e_3^T R_{BM}^B e_3$ with the FSR sensor value f which measures the contact force in the direction normal to $\{C\}$, $K(q) = e_3^T R_{BM}^B e_3 \operatorname{diag}(k_i)$ with the stiffness of each spring $k_i, i \in \{1,2,3\}$, and (q_0, ξ_0) is the initial configuration specified from the free lengths of the springs l_0. This quasi-static analysis is adequate since the inertias of wires, springs, and the contact part are small enough and the motion is not fast in practice. The justification of this extended pose estimator for the contact case is experimentally verified in Sec. IV-A.

C. Hybrid Orientation-Force Control

Due to our modeling of the system with the Pfaffian constraint, we can develop the hybrid orientation-force control

to generate a contact force f^B that is consistent with the desired one f_d^B in both direction and magnitude. This control objective $f^B \to f_d^B$ can be rewritten as

$$q \to q_d, \quad \lambda \to \lambda_d$$

where q_d is the q-value for $R_{BM}^B e_3 = \operatorname{vec}(f_d^B)$ calculated using (3), and $\lambda_d = \|f_d^B\|$. To achieve this, using a hybrid position-force control approach based on the configuration space decomposition (4) and Pfaffian constraint (5), we design the control action u_d as

$$u_d = -K(q)\left[J^\dagger(q - q_0 - K_{o,p}e_q - K_{o,i}\int e_q dt)\right.$$
$$\left. + N_J(\xi - \xi_0)\right] + A^T\left[\lambda - K_{f,p}e_\lambda - K_{f,i}\int e_\lambda dt\right]$$

where $e_q := q - q_d$, $e_\lambda := \lambda - \lambda_d$, and $K_{o,p}, K_{o,i} \in \Re^{2\times 2}$, $K_{f,p}, K_{f,i} \in \Re$ are positive definite parameters. Then the direct torque control $u = u_d$ forms closed-loop dynamics as follows:

1) Orientation control

$$K_{o,p}(q - q_d) + K_{o,i}\int(q - q_d)dt = 0$$

2) Force control

$$K_{f,p}(\lambda - \lambda_d) + K_{f,i}\int(\lambda - \lambda_d)dt = 0$$

where $\lambda = 0$ is measured for contactless case, thus achieving the two control objectives simultaneously.

Finally, we want $u \to u_d$ by applying pulse width modulation (PWM) command to motors. The DC-micromotors of the CHD hardware, however, are coupled with gearheads which causes dead-zone and non-back-drivability due to high friction. To attenuate this friction, we devise the following wire tension regulator:

$$u_m = -K_{m,p}(u - u_d) - K_{m,i}\int(u - u_d)dt$$

where u is the estimated current tension calculated from (6) and $K_{m,p}, K_{m,i} \in \Re$ are positive parameters.

IV. PERFORMANCE EVALUATION

To evaluate the performance of the proposed device and its control framework, we utilize an MCU board (PJRC, Teensy 4.0, ARM Cortex-M7) to operate the CHD hardware. The pose estimation and control are all computed onboard with the control frequency 1 [kHz]. The C++ Eigen library is used for matrix computation.

A. Performance Evaluation of Pose Estimator

Since the feedback control is performed based on the coordinates defined in the kinematics analysis, not a direct measurement for the pose of the CHD, it is necessary to verify the accuracy of the pose estimator derived in Sec. III-A. For the ground truth data acquisition, we use the motion capture system (NaturalPoint, OptiTrack, (measurement error) ≤ 0.2 [mm]) and operate the CHD hardware to which 3D-printed mock-ups with IR markers
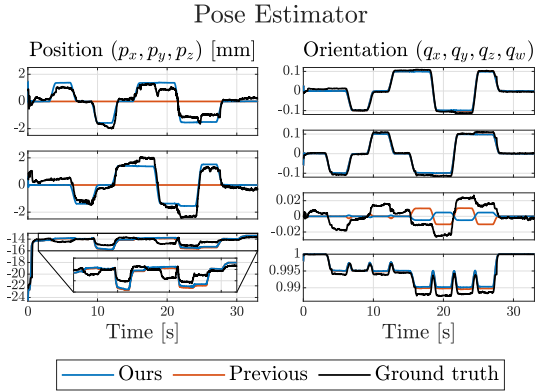
Fig. 6. Comparison of the accuracy of calculated position $p^B_{O_B,O_M}$ (left) and orientation q^B_{BM} (right, in quaternion) for two different pose estimators.

Fig. 8. Performance evaluation for the hybrid orientation-force controller to control contact force direction (q) and magnitude (λ) simultaneously.
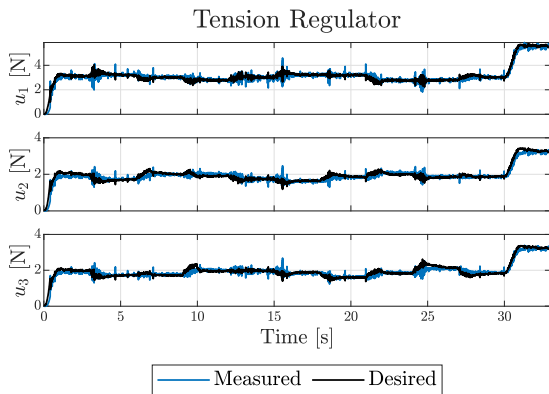

Fig. 7. Performance evaluation for the tension regulator to mitigate the frictional effect generated by the motor gearheads in the CHD hardware.

Fig. 9. Comparison of contact force trajectory tracking performance for two different controllers.

are attached. The trajectory that the CHD travels during the experiment is chosen to cover all reachable configurations: it moves vertically to generate contact with the fingertip, then tilts the contact part, rotate two turns, returns to the initial orientation, and presses the fingertip tighter. We also simultaneously simulate another pose estimator, based on the kinematics analysis presented in [14], for comparison. The experimental results are shown in Fig. 6, where the RMSEs of our estimator are 0.8039 [mm] for position, and 2.1221 [deg] for rotation, while those of the previous work are 1.6260 [mm] and 1.9733 [deg], respectively. Note here that our pose esitmator can capture the horizontal translations (i.e., (e_1, e_2)-components of $p^B_{O_B,O_C}$), which was ignored in the previous work [14] due to the simplifying linearization applied near the initial configuration. This makes our current pose estimator overall much more accurate than the previous one in [14], even though both exhibit similar levels of orientation estimation performance.

B. Performance Evaluation of Controller

Now we verify the proposed controller and the tension regulator in Sec. III-C through experiments on the task of tracking the pre-defined desired contact force trajectory. The
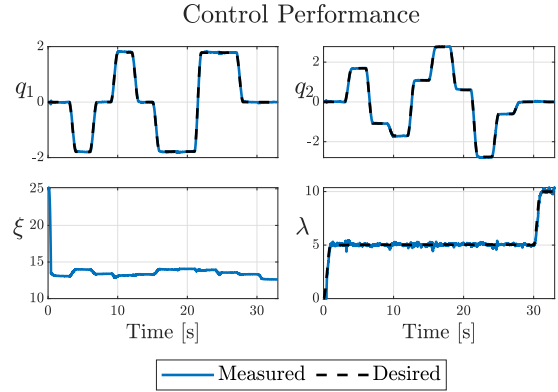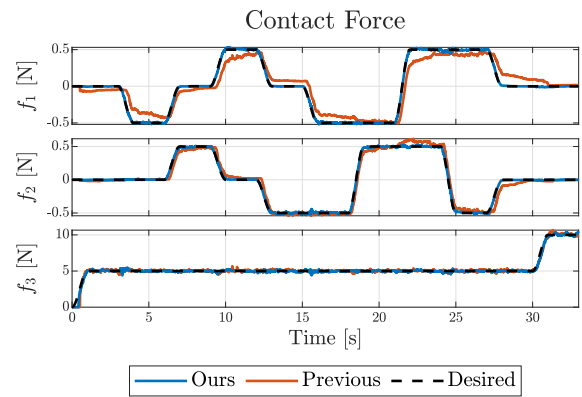
desired force used in the experiment is selected within

$$f^B_d \in \left\{ \begin{bmatrix} f_1; & f_2; & f_3 \end{bmatrix} : \begin{array}{c} |f_1|, |f_2| \leq 0.5\ [\text{N}] \\ 0 \leq f_3 \leq 10\ [\text{N}] \end{array} \right\}$$

which eventually travels along the trajectory used in the experiment in Sec. IV-A. We also compare the performance with the controller proposed in [14] by experimenting on the same desired trajectory. For the control gains used for the experiment, we select $K_{o,p} = 40I_2$, $K_{o,i} = 20I_2$ [s^{-1}], $K_{f,p} = 0.5$, $K_{f,i} = 5$ [s^{-1}], $K_{m,p} = 7$, and $K_{m,i} = 5$ [s^{-1}].

The experimental results show that the proposed control framework can render the desired three-DoF contact force, especially the horizontal component (i.e., f_1, f_2), more accurately than the previous controller, as shown in Fig. 9. The tension of each wire is well stabilized around the target tension (see Fig. 7), allowing the direction (q) and magnitude (λ) of the contact force to track the desired trajectory (see Fig. 8, Fig. 9). We excpect that the relatively noticeable small errors to λ stems mainly from the signal noise of the FSR sensor. The RMSEs measured during the experiment are summarized in Table I, as well as their normalized values calculated by NRMSE = RMSE/$(x_{\max} - x_{\min})$. Since the *measured* contact force used for Fig. 9 and Table I is an

TABLE I

CONTROLLER PERFORMANCE EVALUATION RESULT

(Fig. 7)	Tension		
	u_1	u_2	u_3
RMSE [N]	0.2264	0.1553	0.1555
NRMSE [%]	3.9284	4.5330	4.6216

(Fig. 8)	Orientation		Force
	q_1	q_2	λ
RMSE	0.0259	0.0293	0.1644
NRMSE [%]	0.7224	0.5299	1.6440

(Fig. 9)		Contact Force		
		f_1	f_2	f_3
Ours	RMSE [N]	0.0098	0.0102	0.1642
	NRMSE [%]	0.9758	1.0244	1.6419
Previous	RMSE [N]	0.1156	0.0653	0.2320
	NRMSE [%]	11.5630	6.5319	2.3196

Contact Force

Fig. 11. Performance evaluation of contact force tracking generated by application scenario. Users can feel each shape through the contact force generated when they touch the globe, table, and rabbit in the VR environment. The RMSEs are $\begin{bmatrix} 0.0784; & 0.1261; & 0.7926 \end{bmatrix}$ [N].

interference induced by DC-micromotors. The user wears VIST glove and puts the CHD hardware on the index finger. As the index fingertip touches the surface of the virtual object, a contact force is generated, whose direction is normal to the contact surface and the magnitude is proportional to the penetration depth. The contact force is then saturated to be within the renderable area of the CHD hardware. We use a desktop PC (AMD, Ryzen 5 3600 / NVIDIA, GeForce GTX 1660 Super) with a game engine (Unity Techonologies, Unity) for the VR environment simulation and a head mounted display (Meta, Meta Quest 2) for immersive display.

The experimental results are shown in Fig. 10 and Fig. 11, where the user can touch the virtual objects: a globe and a rabbit, and a table on which they are placed. Since the CHD not only indicates the occurrence of contact but also precisely renders the contact force which changes in real-time according to the posture of the fingers, it provides users with a more realistic and immersive experience.
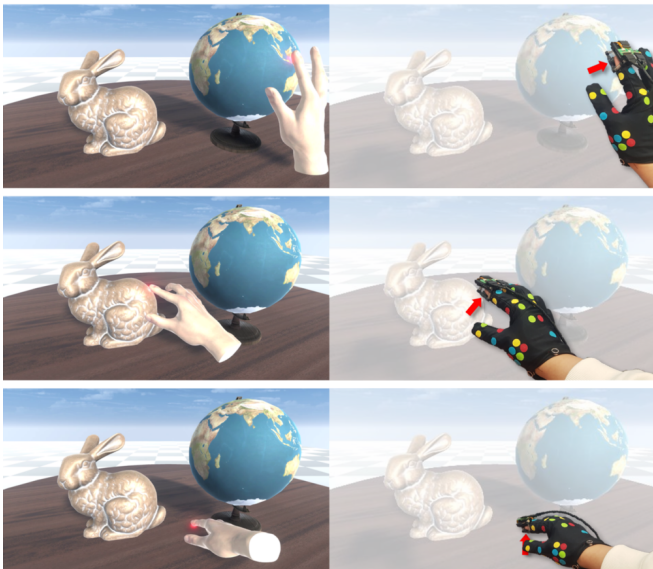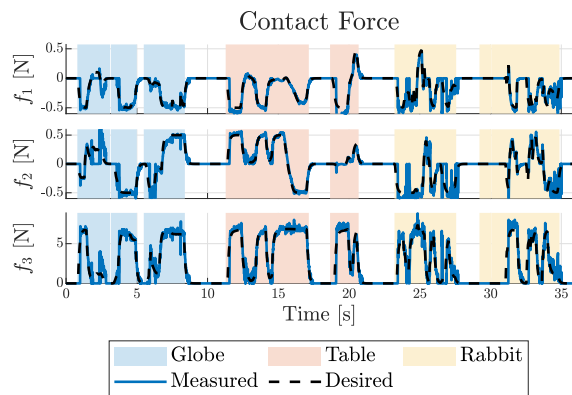

Fig. 10. Snapshots of finger-based virtual object exploration task (left), and photos of the CHD with VIST glove corresponding to each time (right).

estimated value, there may be an error compared to that measured directly through a F/T sensor or the like. However, at least for the estimator we propose, we expect that as long as the assumptions introduced through Sec. III-A and Sec. III-B hold, the accuracy of the contact force direction is ensured by the pose estimator as verified in Sec. IV-A, and the contact force magnitude is measured accurately up to the performance of the FSR sensor. We leave the verification of this hypothesis as a future research topic.

V. ILLUSTRATIVE APPLICATION

As an illustrative application of the proposed device and its control framework, we present a finger-based exploration scenario for the objects in a VR environment. The visual-inertial skeleton tracking (VIST) system proposed in [17] is used for the hand (with thumb, index, middle fingers) motion tracking. Especially, the VIST framework has advantage of being robust to occlusion, electromagnetic interference and contact, making it sutiable for the integration with the CHD: occlusion near the CHD hardware, electromagnetic

VI. CONCLUSION

In this paper, we present novel symmetry-based modeling and hybrid orientation-force control frameworks for wearable CHD to generate precise three-DoF contact force on the fingertip robustly against interuser variability. We analyze the kinematics of the CHD and propose a pose estimator and system modeling by exploiting the symmetrical nature of the device mechanism. We then design a hybrid orientation-force controller to track the direction and magnitude of the desired contact force simultaneously in a feedback manner for control accuracy and robustness. A tension regulator is also adopted to mitigate the frictional effect of the actuators. To verify the proposed framework, we evaluate the performance of the pose estimator and controller against those of the previous work [14], and present an illustrative application: finger-based virtual object exploration.

Some future research directions include: 1) quantitive verification on the performance of the proposed device

with its control framework using direct measurement (e.g., F/T sensor) on generated contact force; 2) application on other haptic scenarios (e.g., teleoperation, VR, AR); and 3) comparison with other haptic devices (e.g., [7]).

REFERENCES

[1] H. A. Sonar, A. P. Gerratt, S. P. Lacour, and J. Paik, "Closed-loop haptic feedback control using a self-sensing soft pneumatic actuator skin," *Soft Robotics*, vol. 7, no. 1, pp. 22–29, 2020.

[2] V. Vechev, J. Zarate, D. Lindlbauer, R. Hinchet, H. Shea, and O. Hilliges, "Tactiles: Dual-mode low-power electromagnetic actuators for rendering continuous contact and spatial haptic patterns in vr," in *2019 IEEE Conference on Virtual Reality and 3D User Interfaces (VR)*, 2019, pp. 312–320.

[3] Y. Lee, S. Lee, and D. Lee, "Wearable haptic device for stiffness rendering of virtual objects in augmented reality," *Applied Sciences*, vol. 11, no. 15, p. 6932, 2021.

[4] C. Pacchierotti, S. Sinclair, M. Solazzi, A. Frisoli, V. Hayward, and D. Prattichizzo, "Wearable haptic systems for the fingertip and the hand: taxonomy, review, and perspectives," *IEEE Transactions on Haptics*, vol. 10, no. 4, pp. 580–600, 2017.

[5] S. R. Williams, J. M. Suchoski, Z. Chua, and A. M. Okamura, "A 4-degree-of-freedom parallel origami haptic device for normal, shear, and torsion feedback," *IEEE Robotics and Automation Letters*, vol. 7, no. 2, pp. 3310–3317, 2022.

[6] S. B. Schorr and A. M. Okamura, "Three-dimensional skin deformation as force substitution: Wearable device design and performance during haptic exploration of virtual environments," *IEEE Transactions on Haptics*, vol. 10, no. 3, pp. 418–430, 2017.

[7] I. Jang and D. Lee, "On utilizing pseudo-haptics for cutaneous fingertip haptic device," in *2014 IEEE Haptics Symposium*, 2014, pp. 635–639.

[8] T. L. Baldi, S. Scheggi, L. Meli, M. Mohammadi, and D. Prattichizzo, "Gesto: A glove for enhanced sensing and touching based on inertial and magnetic sensors for hand tracking and cutaneous feedback," *IEEE Transactions on Human-Machine Systems*, vol. 47, no. 6, pp. 1066–1076, 2017.

[9] D. Leonardis, M. Solazzi, I. Bortone, and A. Frisoli, "A 3-rsr haptic wearable device for rendering fingertip contact forces," *IEEE Transactions on Haptics*, vol. 10, no. 3, pp. 305–316, 2016.

[10] C. Pacchierotti, G. Salvietti, I. Hussain, L. Meli, and D. Prattichizzo, "The hring: A wearable haptic device to avoid occlusions in hand tracking," in *2016 IEEE Haptics Symposium*, 2016, pp. 134–139.

[11] E. R. Serina, E. Mockensturm, C. Mote Jr, and D. Rempel, "A structural model of the forced compression of the fingertip pulp," *Journal of Biomechanics*, vol. 31, no. 7, pp. 639–646, 1998.

[12] D. Prattichizzo, F. Chinello, C. Pacchierotti, and M. Malvezzi, "Towards wearability in fingertip haptics: a 3-dof wearable device for cutaneous force feedback," *IEEE Transactions on Haptics*, vol. 6, no. 4, pp. 506–516, 2013.

[13] F. Chinello, M. Malvezzi, D. Prattichizzo, and C. Pacchierotti, "A modular wearable finger interface for cutaneous and kinesthetic interaction: control and evaluation," *IEEE Transactions on Industrial Electronics*, vol. 67, no. 1, pp. 706–716, 2019.

[14] Y. Lee, M. Kim, Y. Lee, J. Kwon, Y.-L. Park, and D. Lee, "Wearable finger tracking and cutaneous haptic interface with soft sensors for multi-fingered virtual manipulation," *IEEE/ASME Transactions on Mechatronics*, vol. 24, no. 1, pp. 67–77, 2018.

[15] B. Gao, H. Song, J. Zhao, S. Guo, L. Sun, and Y. Tang, "Inverse kinematics and workspace analysis of a cable-driven parallel robot with a spring spine," *Mechanism and Machine Theory*, vol. 76, pp. 56–69, 2014.

[16] B. Gao, Z. Zhu, J. Zhao, and L. Jiang, "Inverse kinematics and workspace analysis of a 3 dof flexible parallel humanoid neck robot," *Journal of Intelligent & Robotic Systems*, vol. 87, pp. 211–229, 2017.

[17] Y. Lee, W. Do, H. Yoon, J. Heo, W. Lee, and D. Lee, "Visual-inertial hand motion tracking with robustness against occlusion, interference, and contact," *Science Robotics*, vol. 6, no. 58, p. eabe1315, 2021.